



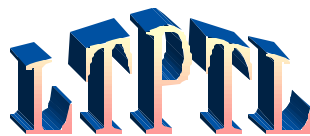
Low Temperature Plasma Technology Laboratory

PLASMA INJECTION WITH HELICON SOURCES

Francis F. Chen, Xicheng Jiang, and John D. Evans
Electrical Engineering Department, UCLA

LTP-907

July, 1999



Electrical Engineering Department
Los Angeles, California 90095-1594

Plasma Injection with Helicon Sources

Francis F. Chen , Xicheng Jiang, and John D. Evans

Electrical Engineering Department, University of California, Los Angeles, California 90095-1594

ABSTRACT

An exhaustive set of measurements has been made to find the optimum conditions for plasma injection into a processing chamber using small helicon sources with low magnetic fields B . It is found that the plasma density decreases with B , rather than increasing, as it does in normal helicon discharges. The design of the field coil and flange caused this effect; with a different design, normal operation was obtained. This experiment provides data on the area coverage of individual helicon discharges for the design of large-area, distributed plasma sources.

I. INTRODUCTION

Helicon sources are known for their ability to produce dense, uniform plasmas for semiconductor etching and deposition¹. We have previously shown that multiple helicon sources can be used to cover large substrates uniformly^{2,3}. The data presented here were taken prior to that work to determine the coverage provided by each individual small source. As guides to our design, we used three features of helicon discharges found in previous work: 1) the plasma density n has a peak at low magnetic fields in the 20-50G range⁴, 2) the density n peaks not under the antenna but downstream from it⁵, and 3) helical antennas exciting right-hand circularly polarized waves yield the highest densities⁵. An example of the low-field peak is shown in Fig. 1. A peak in plasma loading resistance at these low fields is predicted by the theory of Arnush and Chen⁶ and has been attributed to the strong damping of Trivelpiece-Gould (electron cyclotron) waves, which couple well to helicon waves at low fields. The downstream peak and the superiority of the R-antenna are shown by the bifilar-antenna data of Fig. 2. In the present experiment, single $m = 1$ helical antennas were used, where m is the azimuthal mode number, so that right-hand rotation could be produced by spatial but not temporal rotation; nonetheless, the top curve of Fig. 2 approximates what is obtained with a single RH antenna. The rise in density downstream from the antenna has been explained⁷ by pressure balance ($nKT_e = \text{constant}$) along B as the electron temperature T_e decays away from the antenna. The decrease in n far downstream is due to radial losses. The downstream peak has also been observed in the nonuniform magnetic field of a processing reactor¹. The result of the present work was that although high densities typical of helicon discharges were produced, the low-field peak (Fig. 1) was not observed; increasing B actually had a deleterious effect. We show that this was caused by magnetic field coils that were too tightly coupled to the discharge tube. Tests with larger coils reproduced the low-field peak and the expected behavior of normal helicon discharges.

II. APPARATUS

Measurements were carried out in the 30-cm diam chamber shown in Fig. 3. A detail of the 5-cm diam, 15 cm long source tube is shown in Fig. 4. The 10 cm long, half-

wavelength antenna is driven by 0-2000W of pulsed RF at either 13.56 or 27.12 MHz. The antenna helicity and magnetic field direction combined to launch $m = +1$ waves downwards into the chamber. For each radial scan the matching circuit was manually tuned to reduce reflected power below 0.1%. Argon gas is fed into the main chamber. The magnet coils, approximately 12 cm long, are made of 400 turns of Formvar[®]-coated AWG #28 wire wound on a plastic cylinder about 8 cm in diameter. A small DC power supply suffices for fields up to 100G. Densities are measured with saturation ion current to uncompensated Langmuir probes calibrated against a microwave interferometer. A PMT FastProbe[®] (not shown) was substituted for the straight probe to obtain radial profiles in about one second. Data were averaged over six scans.

III. MEASUREMENTS : STANDARD CONFIGURATION

Figs. 5 and 6 show the peak densities at 13.56 and 27.12 MHz. All data are for 18 mTorr of argon and probe position $z = 6$ cm, unless otherwise noted. It is seen that the highest density is at $B = 0$, there being no evidence of the low-field peak seen in Fig. 1. Nonetheless, the density reaches $2 \times 10^{12} \text{ cm}^{-3}$ even in ICP operation at $B = 0$. The higher frequency yields higher density here since the antenna was designed for 27 MHz.

Figs. 7 and 8 show, respectively, the radial density profiles at 13.56 and 27.12 MHz for various magnetic fields. Figs. 9 and 10 show the same as a function of RF power. One sees that the profiles are all quite similar, regardless of the magnetic field. The pressure dependence was then studied, and the density profiles at two frequencies are shown in Fig. 11 for 0 G and 600 W. The peak density as a function of pressure (from a different run) is plotted in Fig. 12. Note that the discharge is unstable at the lowest pressure at 13.56 MHz. The pressures here are the filling pressures before the discharge is ignited. During the discharge, the pressure in the source tube can be considerably lower because of gas depletion. The peak density 6 cm downstream initially rises with pressure, then falls because of increased diffusion. At high pressures, n levels off as more gas is able to penetrate into the source tube. The peculiar behavior at 13.56 MHz may have been caused by instabilities.

IV. MEASUREMENTS: ALTERNATE CONFIGURATIONS

Diffusive spreading of the plasma can be seen from profiles taken near the source at $z = 0.5$ cm and at the normal position of 6 cm, as shown in Fig. 13 for 13.56 and 27.12 MHz. Note that the scales are different. The unnormalized peak $n(B)$ curves for these positions at various RF powers are shown in Fig. 14. There is a monotonic decrease in density with B in all cases.

At this point it was thought that the region of uniform magnetic field was not long enough for helicon waves to be excited, causing the absence of the low-field peak seen in normal helicon discharges. To test this, we lengthened the magnetic field by a factor of two in the modified device shown in Fig. 15. The resulting $n-B$ curve is shown in Fig. 16. It is seen that n no longer falls with B but still does not peak. The curve for the short tube is shown for comparison, but the magnitudes should not be compared because the data were taken in different epochs.

The effect of a magnetic bucket, an array of permanent magnets on the outside surface of the main chamber, was tested next. These magnets form magnetic line cusps which reflect electrons which impinge on the wall at an angle. These surface fields extend only a small distance into the chamber and leave the most of the volume field-free. Because of collisions, fast electrons are confined better than slow electrons, which may scatter into a

loss orbit while inside the cusp region. Measurements were taken at $z = 6$ cm with and without the bucket array at 600, 1000, and 1400 W and B -fields of 0, 25, and 50 G. Since the results were similar, only the data at 1400 W are shown in Fig. 17. It is seen that the bucket does not increase the peak density, but does raise the density near the wall.

Other antenna configurations were also tested, and the $n - B$ curves for 27.12 MHz and 18 mTorr are shown in Fig. 18(a-g). Each graph is labeled with the antenna type. The right-helical case is shown in Fig. 6. A Nagoya Type III antenna has straight, rather than helical, legs and excites both right- and left-polarized helicon waves, though only the former is found to propagate well. A Boswell antenna, or double saddle coil antenna, has four straight legs, with the current direction in a + + - - order. These three antennas are all of $m = 1$ azimuthal symmetry. A two-ring $m = 0$ antenna has two simple loops, separated by 5 or 10 cm, with the current in opposite directions in each ring. A one-ring antenna is a single turn which can be placed at the midplane of the source tube, or 3 cm below or above it. The right-helical and Nagoya Type III antennas are generally equally effective, with the RH antenna being somewhat better, though the present data favor the Nagoya antenna. The double-saddle coil produces a little less density. Figure 19 compares all antennas at 1kW power. The wildly different results for the various $m = 0$ configurations, including some that show a low-field peak, indicate that there are many complicating factors at play here, but the best of these configurations compare favorably with the $m = 1$ configurations.

V. ANALYSIS AND DISCUSSION

The reason for the density falling monotonically with magnetic field can be seen when one plots carefully the magnetic field of the small solenoid, as is shown in Fig. 20. The two flanges are so thick that many of the field lines in the tube intersect the flange opening or turn back to strike the underside of the top plate. At $B = 0$, the plasma diffuses isotropically from the source, but as the magnetic field is raised, the electrons become more and more magnetized and begin to follow the lines of force. In doing so, they set up ambipolar electric fields which force the unmagnetized ions to follow the field lines also. At high magnetic fields, only a fraction of the plasma streaming from the source can reach the downstream region; namely, the part created near the axis in the source tube. Also shown in Fig. 20 are the sizes of the Larmor orbits downstream when $B = 100$ G in the source. Even at this highest field, the downstream orbits become larger than the scalelength of the magnetic field. Because of this, and because of the short-circuit effect at wall sheaths, modeling the density profiles would require a sophisticated code which is outside the scope of this work.

Nonetheless, our results can be explained qualitatively by simple calculations. Consider first the ICP case, $B = 0$. The plasma leaves the source and enters the main chamber with a drift velocity v_0 . Except for a small amount of downstream ionization and scattering of ions against neutral argon atoms, there are no ions traveling back into the source tube. The drift velocity must then satisfy the Bohm sheath criterion,

$$v_0 \geq c_s \equiv (KT_e/m)^{1/2}, \quad (1)$$

where c_s is the ion acoustic speed. Upon entering the chamber, plasma normally will diffuse isotropically with the ambipolar diffusion coefficient

$$D_a \approx D_{i0}(1+T_e/T_i), \quad (2)$$

where D_{i0} is the diffusion coefficient for ion-neutral collisions. Note, however, that the injection of plasma with velocity c_s into an existing plasma may cause instabilities resulting

in turbulent diffusion, as would occur with a jet of water or air. The profiles calculated below do not depend on the exact value of D_a . In steady state, the equation of continuity is

$$\nabla \cdot (nv) = 0, \text{ where } nv = -D_a \nabla n. \quad (3)$$

In cylindrical symmetry, the density n then satisfies

$$\frac{\partial^2 n}{\partial r^2} + \frac{1}{r} \frac{\partial n}{\partial r} + \frac{\partial^2 n}{\partial z^2} = 0. \quad (4)$$

Consider a semi-infinite half-space bounded at the top, with z increasing downwards. The flux of plasma $n_0 v_0$ into this volume is through a hole of radius $r = a$. Thus, the boundary condition is

$$\frac{\partial n}{\partial z} = -\frac{n_0 v_0}{D_a} \text{ for } r < a \text{ and } = 0 \text{ otherwise.} \quad (5)$$

The solution of Eqs. (4) and (5) can be found in standard texts on heat conduction⁸:

$$n(r, z) = \frac{n_0 v_0 a}{D_a} \int_0^\infty e^{-Iz} J_0(Ir) J_1(Ia) (dI / I), \quad (6)$$

where J_0 and J_1 are Bessel functions. Since this does not account for the radial density profile within the source, we have used $a = 2$ cm, slightly smaller than the actual radius of 2.5 cm. Fig. 21 shows the value of the integral at various z 's. In Fig. 22, the curves for $z = 0.5$ and 6.0 cm are compared with the 27 MHz data of Fig. 13. It is entirely reasonable that the experimental points at $z = 6$ cm should lie above the theoretical curve, since the theory assumes constant D_a , whereas in practice D_a decreases with z as T_e falls due to inelastic collisions⁷. The agreement in Fig. 22 shows that our physical picture of the $B = 0$ case is roughly correct.

We cannot treat the intermediate case, but we can consider the opposite limit, $B \rightarrow \infty$, in which the injected plasma will follow the magnetic field lines shown in Fig. 20. Each field line originating a radius R_0 at the midplane of the coil will map into a larger radius $R(z)$ for $z > 0$. This mapping $R(R_0)$ is shown in Fig. 23 for the two probe positions z . We see that plasma reaching the downstream probe must have originated at $R_0 < 1.5$ cm. Also shown in Fig. 23 is the angle q of the field line with respect to the z axis. If we assume that ions stream along each field line with constant velocity v_0 , that $n(R_0) \approx \text{constant}$ for $R_0 < 1.5$ cm, and that ion flux is conserved, we can compute the densities at $z = 0.5$ and 6.0 cm ($z_0 = 10.6$ and 16.1 cm) relative to n_0 at $z_0 = 0$. These densities and their ratio are shown in Fig. 24. Note that $n(16)$ peaks at large radii where $q = 90^\circ$ and the downward flow stagnates. This would not occur in practice because the field would be too weak to confine the plasma, but in any case this point occurs outside the chamber. Fig. 24 shows that the ratio $n(16)/n(11)$ should be of order 25%. This result can be compared with the measured ratio of peak densities shown in Fig. 25, which tends toward 35% as B is increased, at least at the lower powers. Only fair agreement is achieved with this rough calculation, but radial profile effects would bring the results closer together. To compare the $B = 0$ and $B \rightarrow \infty$ cases, we can estimate that the density would fall by approximately the ratio of source areas available; namely, $(1.5\text{cm})^2 / (2.5\text{cm})^2 = 0.36$. This compares favorably with the experimental data shown in Fig. 26 for the downstream probe. Integration over the radial profile is not warranted, since the profiles are quite similar.

VI. OPERATION WITH LARGE MAGNETIC COIL

To verify that the magnetic field configuration affected the results, a few measurements were taken under almost identical conditions with the small solenoid replaced by a large coil, shown in Fig. 27, which produced a more uniform field. The resulting $n - B$ curve in Fig. 28 indeed shows the low-field peak. By reversing the direction of \mathbf{B} , it is possible to launch $m = -1$ (left-hand) helicon waves downward with the same antenna. As seen from the lower curve in Fig. 28, this mode is much less efficient in producing plasma. The asymmetry in behavior distinguishes helicon discharges from unmagnetized ICPs. Fig. 29 shows a direct comparison of the two magnetic configurations with all else remaining constant. This was done using a symmetric $m = 0$ antenna, which gives the same result with either direction of \mathbf{B} . Though a distinct low-field peak is not seen here, it is clear that the decrease of density with B does not occur with a more uniform field.

In summary, we have shown that it is possible to create dense helicon plasmas in small tubes and inject them into a diffusion chamber. However, the flanges and magnetic field coils should be designed so that the all of the field lines in the source extend into the downstream region without encountering an obstacle. The measured data are consistent with a qualitative treatment of the plasma expansion.

This work was supported by the National Science Foundation and the Semiconductor Research Corporation.

FIGURE CAPTIONS

- Fig. 1. Density vs. magnetic field, showing a low-field peak (Ref. 1).
- Fig. 2. Axial density variation in a long, uniform helicon plasma. The bifilar helical antenna could be phased to give right- or left-hand rotation in time (RT, LT) or in space (RS, LS) [Ref. 2].
- Fig. 3. Schematic of the apparatus. The source tube is 5 cm and the large chamber approximately 30 cm in diameter. The probe tips are 0.5 and 6.0 cm below the top flange. A permanent magnet array (not shown) can also be placed around the periphery of the chamber to form a magnetic bucket.
- Fig. 4. Detail of the helicon source.
- Fig. 5. Density on axis vs. magnetic field for various RF powers at 13.56 MHz. Unless otherwise specified, all data are for $z = 6$ cm and 18 mTorr of Ar.
- Fig. 6. Density on axis vs. magnetic field for various RF powers at 27.12 MHz.
- Fig. 7. Radial density profiles at 18 mTorr, 13.56 MHz, and various magnetic fields. Each curve consists of 500 data points, and it is not practical to code them. However, the curves appear in the same order as in the legend. To avoid clutter, some curves are not drawn, though they are listed in the right order in the legend. Small oscillations near the axis are due to mechanical vibration of the probe shaft and should be ignored.
- Fig. 8. Radial density profiles at 18 mTorr, 27.12 MHz, and various magnetic fields. Each curve consists of 500 data points, and it is not practical to code them. However, the curves appear in the same order as in the legend.
- Fig. 9. Radial density profiles at 18 mTorr, 13.56 MHz, and various RF powers. Each curve consists of 500 data points, and it is not practical to code them. However, the curves appear in the same order as in the legend. Small oscillations near the axis are due to mechanical vibration of the probe shaft and should be ignored.
- Fig. 10. Radial density profiles at 18 mTorr, 27.12 MHz, and various RF powers. Each curve consists of 500 data points, and it is not practical to code them. However, the curves appear in the same order as in the legend.
- Fig. 11. Radial density profiles as a function of pressure at 13.56 and 27.12 MHz, 600 W, and 0 G. To avoid clutter, not all curves have been drawn; however, those that are shown appear in the same order as in the legend.
- Fig. 12. Peak density as a function of pressure at two frequencies.
- Fig. 13. Radial density profiles at $z = 0.5$ and 6 cm for two frequencies at $B = 0$, 600 W, and 18.4 mTorr. The curves have been renormalized to show the spreading of the profile.
- Fig. 14. Maximum density vs. B at $z = 0.5$ cm (solid points) and 6.0 cm for various powers at 18.4 mTorr and 27.12 MHz.
- Fig. 15. Schematic of long-tube experiment.
- Fig. 16. Density vs. magnetic field for single- and double-length tubes.
- Fig. 17. Radial density profiles at three magnetic fields with (w, thick curves) and without (w/o, thin curves) a magnetic bucket in the experimental chamber. The curves are listed in the legend in the same order as they appear at the right of the graph.
- Fig. 18. Density vs. magnetic field and power for various antennas, as explained in text.
- Fig. 19. Comparison of various antenna types at 1 kW power.

- Fig. 20. Magnetic field lines in the present experiment. The arrows indicate the positions of the probes. The ellipses show the approximate sizes of the electron Larmor diameters at various positions when the field in the source on axis is 100G.
- Fig. 21. Computed density profiles at various positions z for isotropic diffusion with $B = 0$.
- Fig. 22. Calculated diffusive radial profiles compared with the data of Fig. 13.
- Fig. 23. Radius of field line at the probe positions $z_0 = 10.6$ and 16.1 cm from coil midplane ($z = 0.5$ and 6.0 cm from top flange), as function of midplane radius R_0 (hollow points). Also shown is $B_z/B = \cos \mathbf{q}$, where \mathbf{q} is the angle of the field line with the z axis (solid points).
- Fig. 24. Computed densities at the two probe positions and their ratio (solid line) for the case $B \rightarrow \infty$.
- Fig. 25. Ratio of peak densities at $z = 6$ and 0.5 cm as function of magnetic field and power at 27.12 MHz (from data of Fig. 14).
- Fig. 27. Schematic of apparatus with large magnetic field coil.
- Fig. 28. Density vs. magnetic field with a helical antenna and the large field coil shown in Fig. 27.
- Fig. 29. Comparison between $n - B$ curves taken with a small solenoid and with a large coil, taken with an $m = 0$ antenna.

REFERENCES

- ¹ G.R. Tynan, A.D. Bailey III, G.A. Campbell, R. Charatan, A. de Chambrier, G. Gibson, D.J. Hemker, K. Jones, A. Kuthi, C. Lee, T. Shoji, and M. Wilcoxson, *J. Vac. Sci. Technol. A* **15**, 2885 (1997).
- ² F.F. Chen, X. Jiang, J.D. Evans, G. Tynan, and D. Arnush, *Plasma Phys. Control. Fusion* **39**, A411 (1997).
- ³ F.F. Chen and J.D. Evans, *Proc. Plasma Etch Users Group (NCCAUS, 150 W. Iowa Ave., Suite 104, Sunnyvale, CA 94086)* (1998).
- ⁴ F.F. Chen, *Vac. Sci. Technol. A* **10**, 1389 (1992).
- ⁵ D.G. Miljak and F.F. Chen, *Plasma Sources Sci. Technol.* **7**, 61 (1998).
- ⁶ D. Arnush and F.F. Chen, *Phys. Plasmas* **5**, 1239 (1998).
- ⁷ I.D. Sudit and F.F. Chen, *Plasma Sources Sci. Technol.* **5**, 43 (1996).
- ⁸ Carslaw, H.S. and Jaeger, J.C., *Conduction of Heat in Solids* (Oxford Univ. Press, 1959), pp. 214-215.

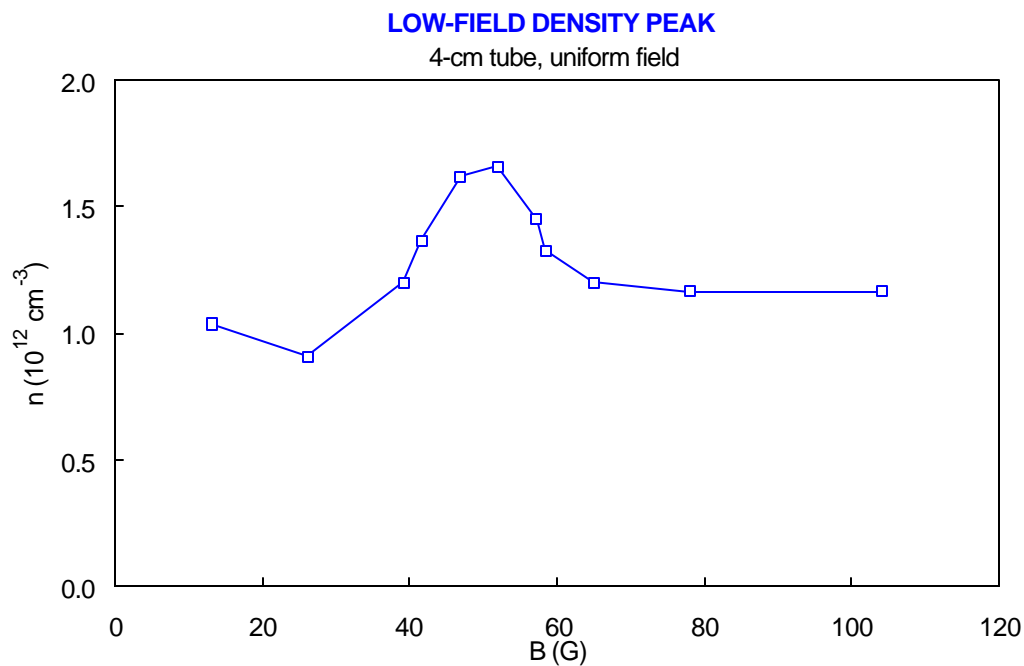


Fig. 1. Density vs. magnetic field, showing a low-field peak [Ref. 1].

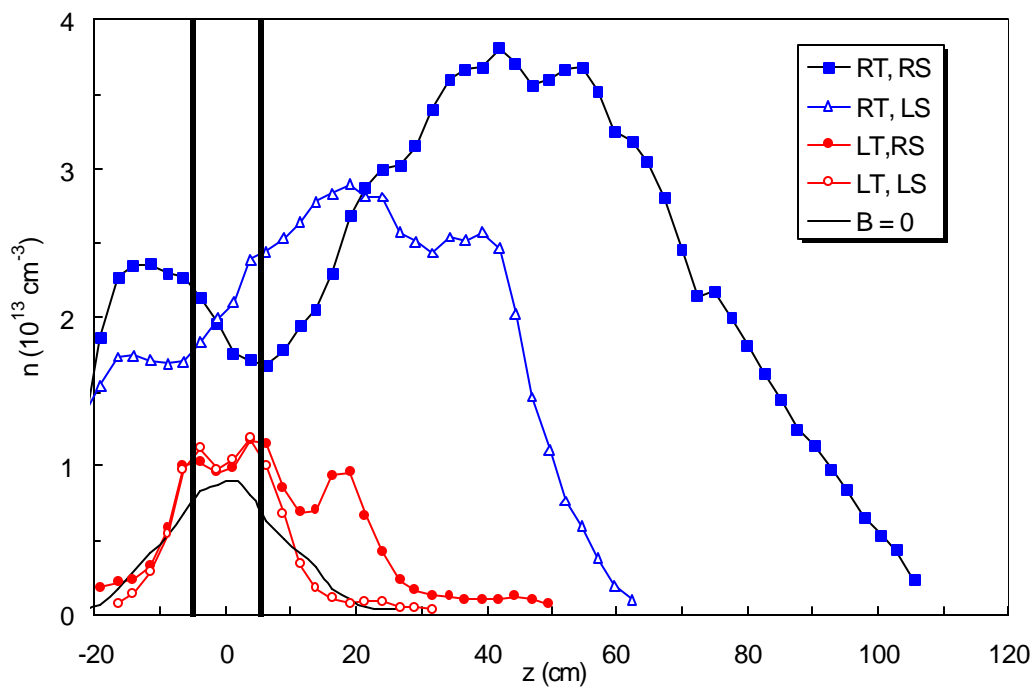


Fig. 2. Axial density variation in a long, uniform helicon plasma. The bifilar helical antenna could be phased to give right- or left-hand rotation in time (RT, LT) or in space (RS, LS) [Ref. 2].

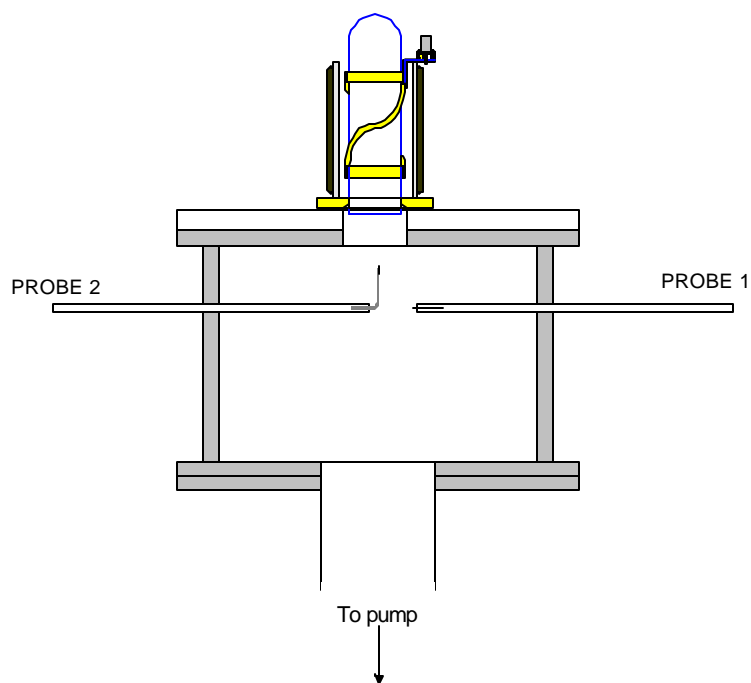


Fig. 3. Schematic of the apparatus. The probe tips are at $z = 0.5$ and 6.0 cm below the top flange. A permanent magnet array (not shown) can also be placed around the periphery of the chamber to form a magnetic bucket.

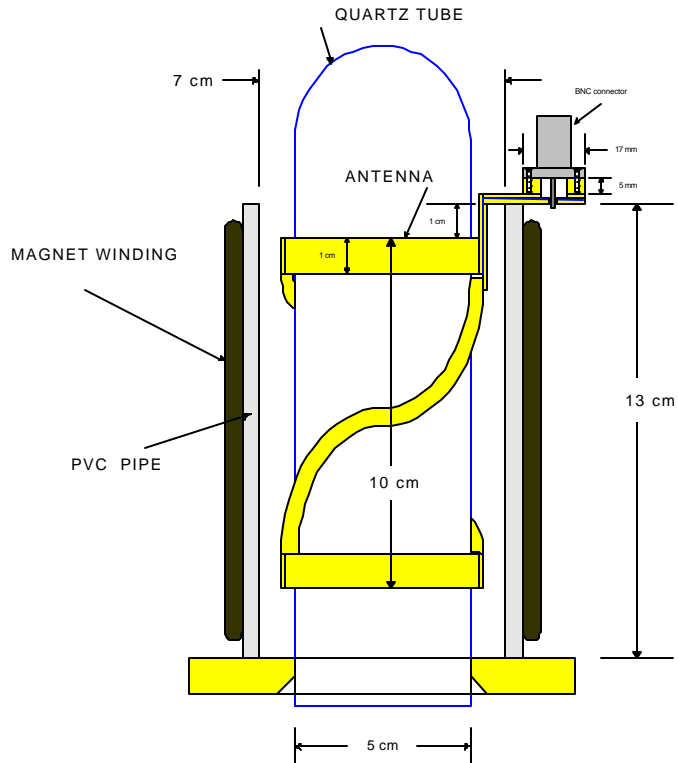


Fig. 4. Detail of the helicon source.

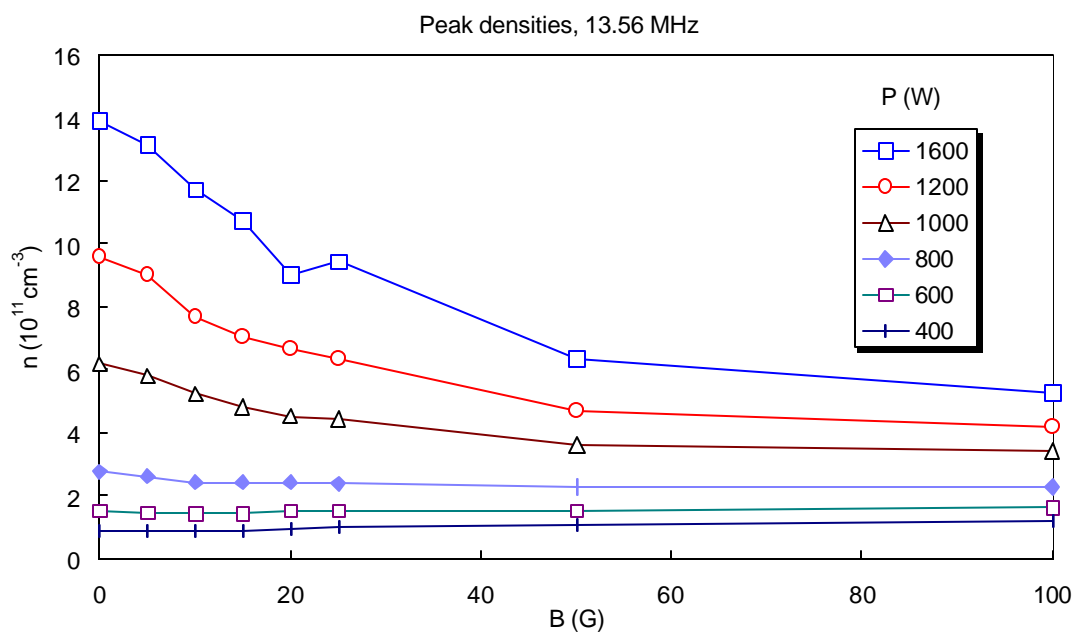


Fig. 5. Density on axis vs. magnetic field for various RF powers at 13.56 MHz. Unless otherwise specified, all data are for $z = 6$ cm and 18 mTorr of Ar.

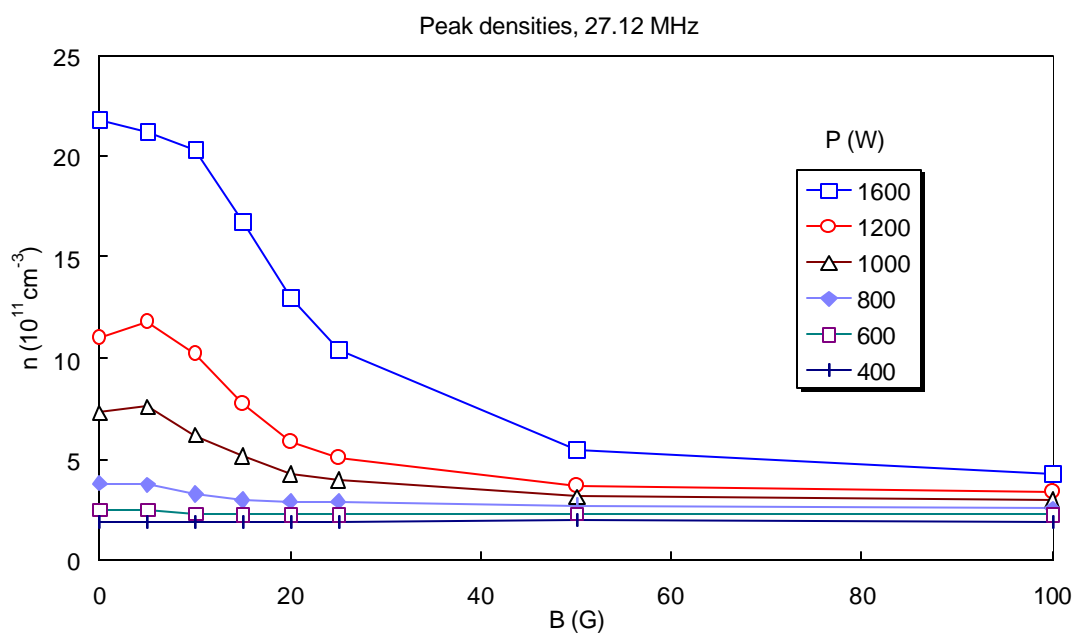


Fig. 6. Density on axis vs. magnetic field for various RF powers at 27.12 MHz.

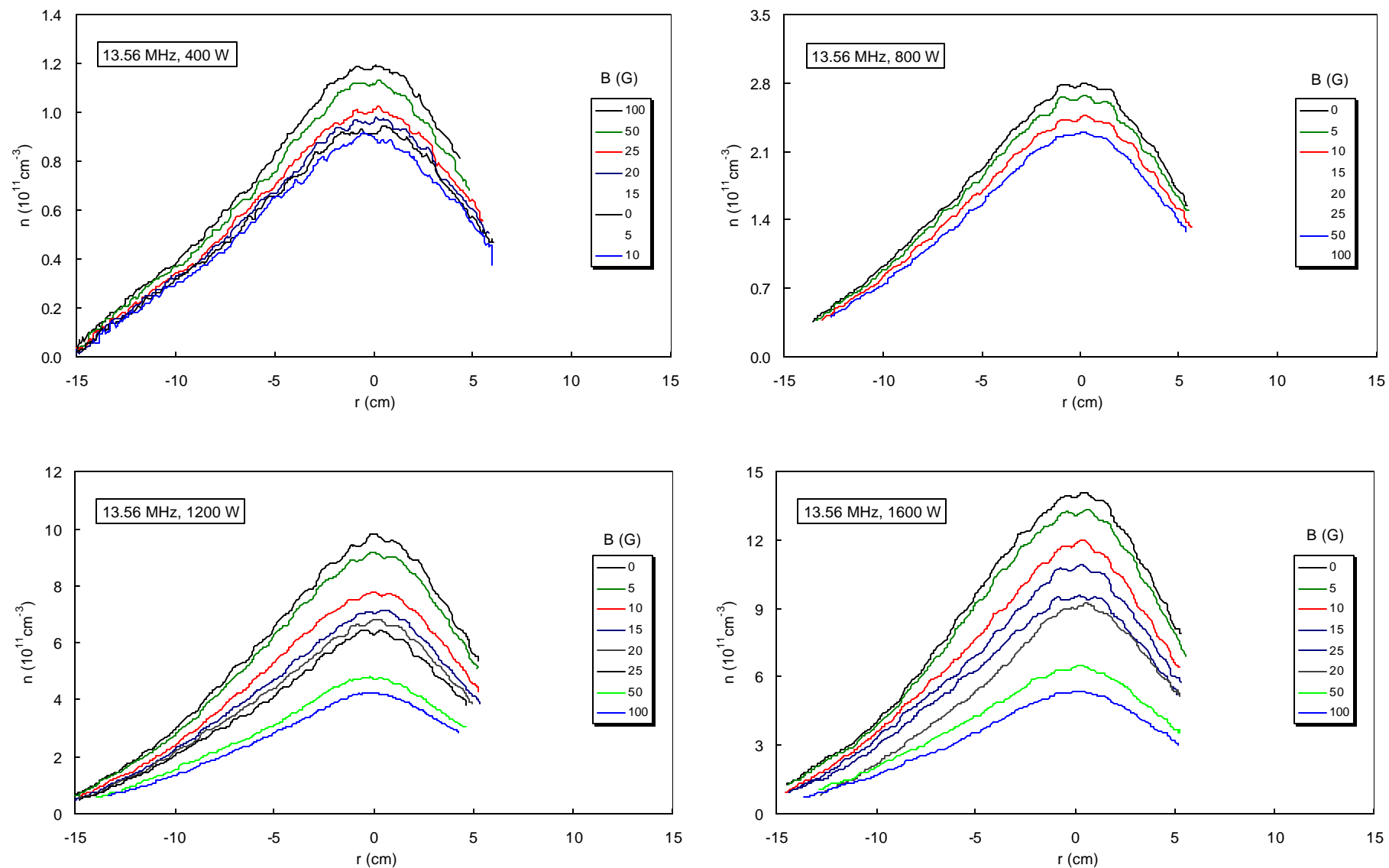


Fig. 7. Radial density profiles at 18 mTorr, 13.56 MHz, and various magnetic fields. Each curve consists of 500 data points, and it is not practical to code them. However, the curves appear in the same order as in the legend. To avoid clutter, some curves are not drawn, though they are listed in the right order in the legend. Small oscillations near the axis are due to mechanical vibration of the probe shaft and should be ignored.

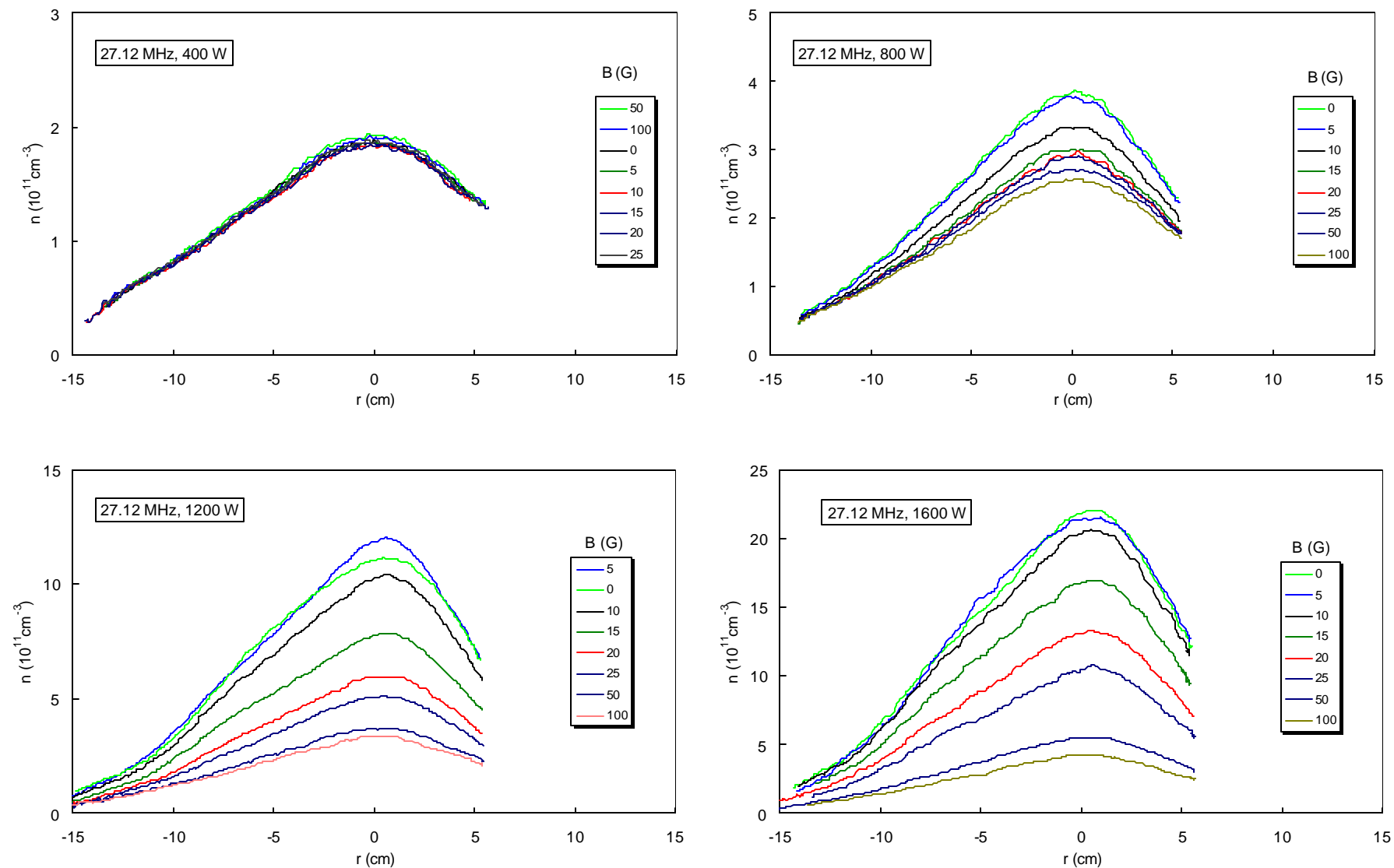


Fig. 8. Radial density profiles at 18 mTorr, 27.12 MHz, and various magnetic fields. Each curve consists of 500 data points, and it is not practical to code them. However, the curves appear in the same order as in the legend.

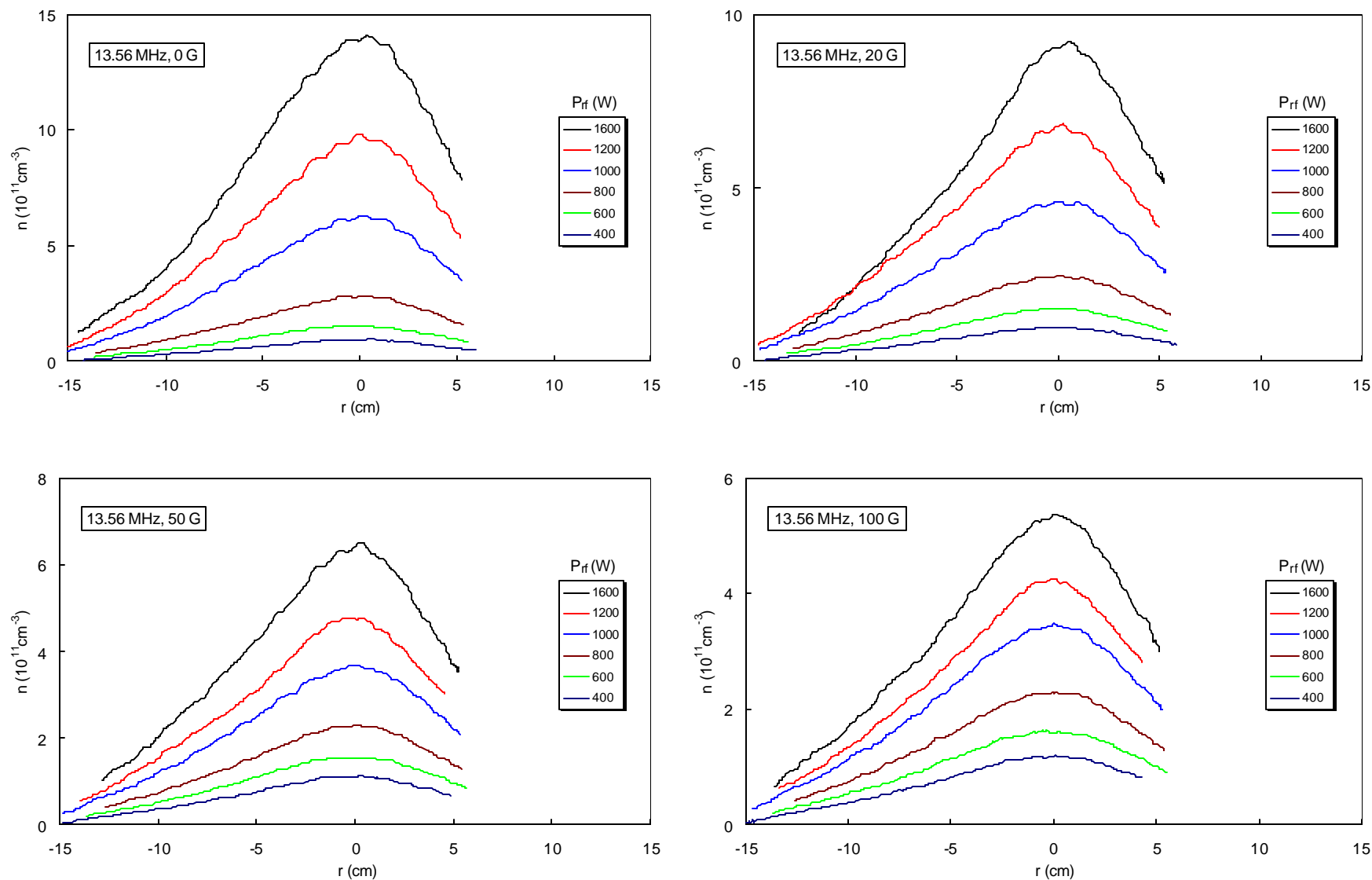


Fig. 9. Radial density profiles at 18 mTorr, 13.56 MHz, and various RF powers. Each curve consists of 500 data points, and it is not practical to code them. However, the curves appear in the same order as in the legend. Small oscillations near the axis are due to mechanical vibration of the probe shaft and should be ignored.

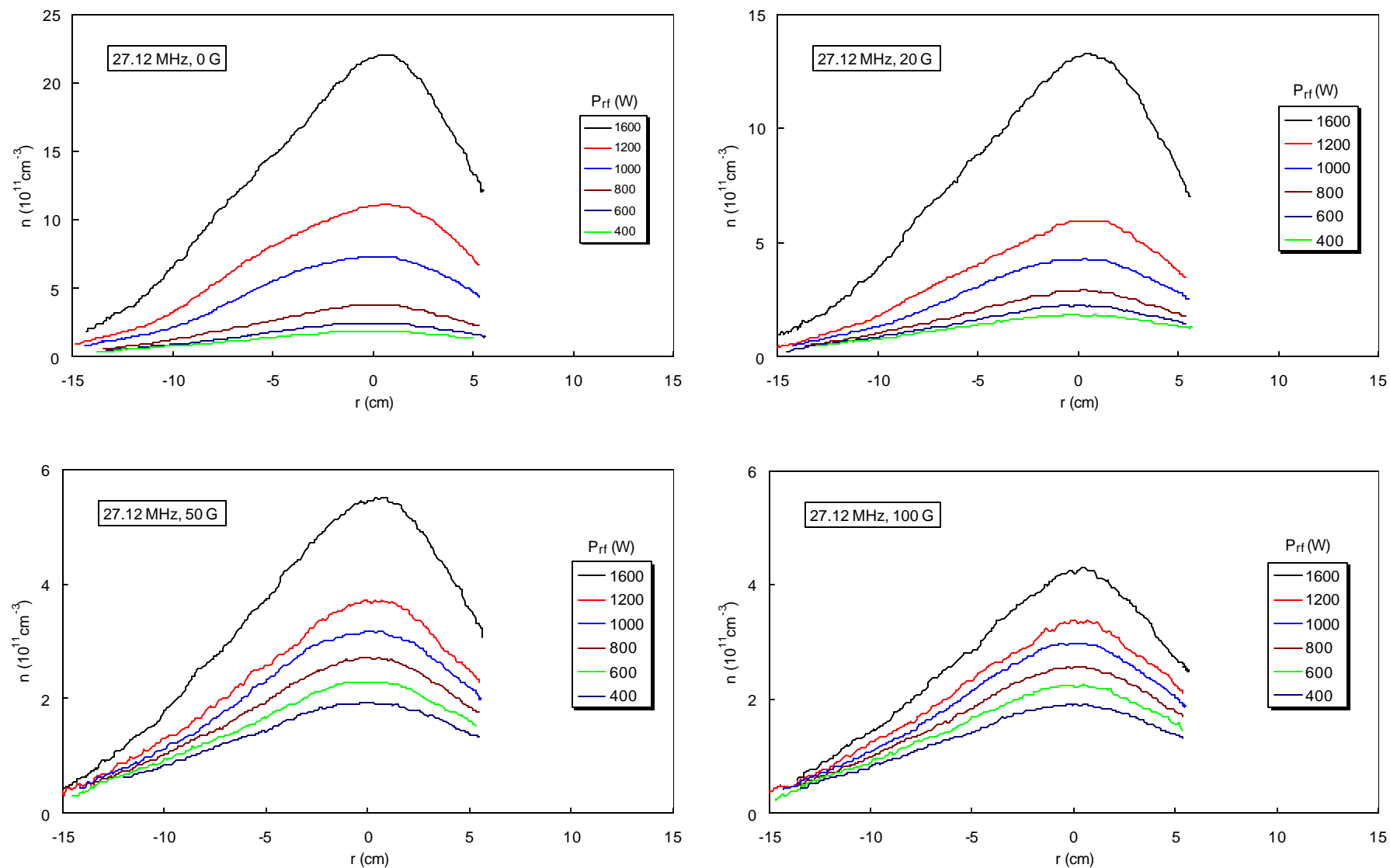


Fig.10. Radial density profiles at 18 mTorr, 27.12 MHz, and various RF powers. Each curve consists of 500 data points, and it is not practical to code them. However, the curves appear in the same order as in the legend.

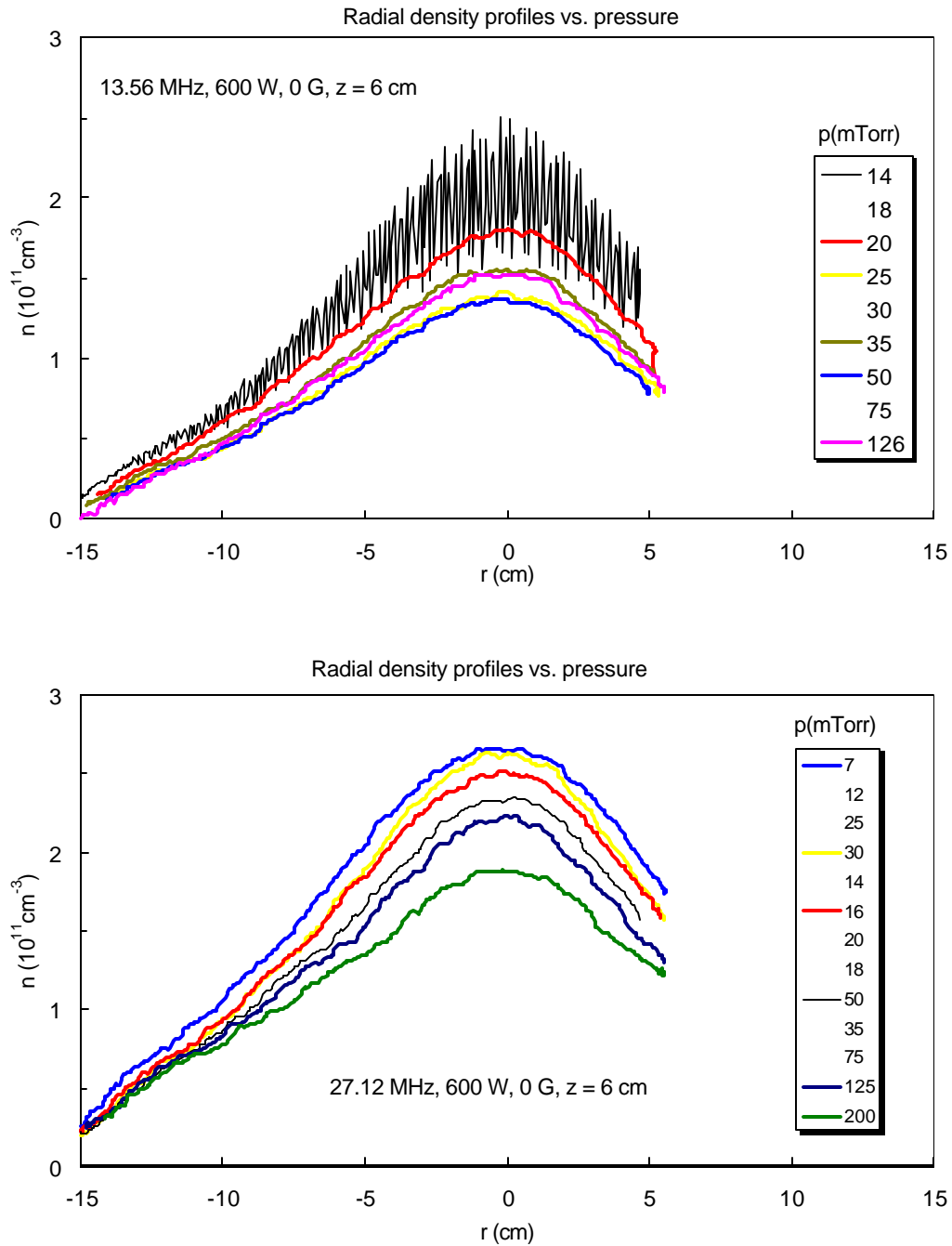


Fig. 11. Radial density profiles as a function of pressure at 13.56 and 27.12 MHz, 600 W, and 0 G. To avoid clutter, not all curves listed in the legend have been drawn; however, those that are shown appear in the same order as in the legend.

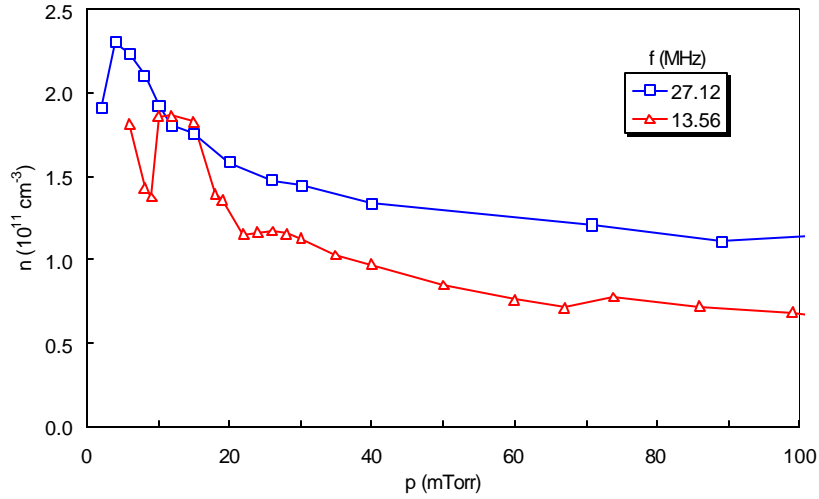


Fig. 12. Peak density as a function of pressure at two frequencies.

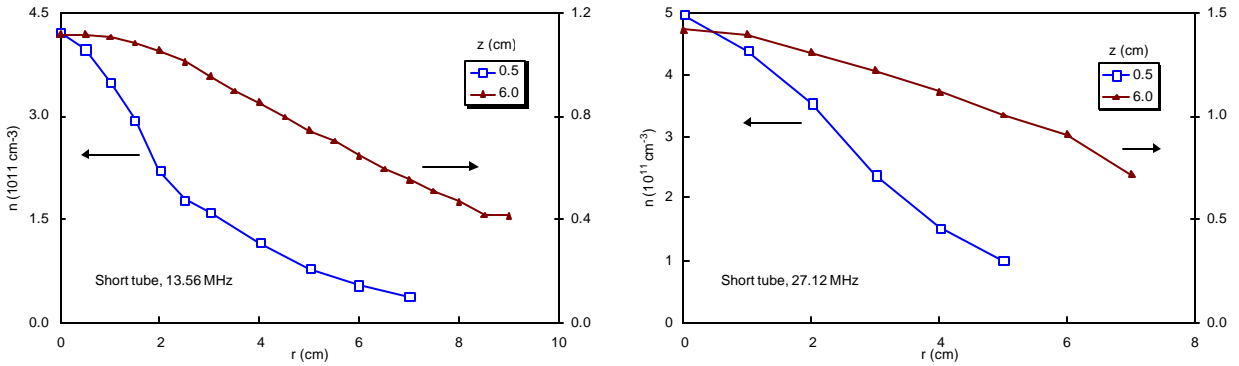


Fig. 13. Radial density profiles at $z = 0.5$ and 6 cm for two frequencies at $B = 0$, 600 W, and 18.4 mTorr. The curves have been renormalized to show the spreading of the profile.

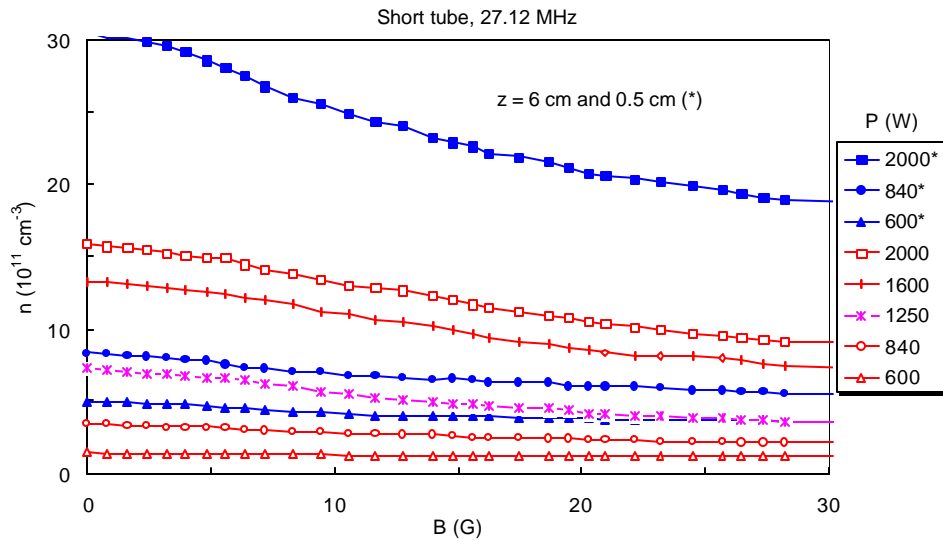


Fig. 14. Maximum density vs. B at $z = 0.5$ cm (solid points) and 6.0 cm for various powers at 18.4 mTorr and 27.12 MHz.

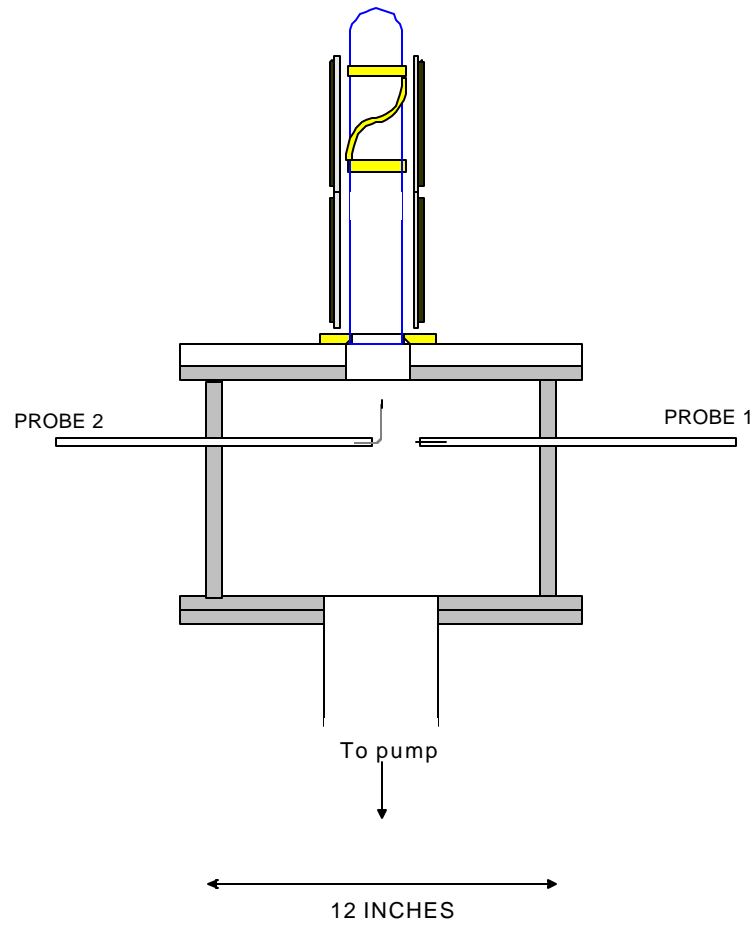


Fig. 15. Schematic of long-tube experiment.

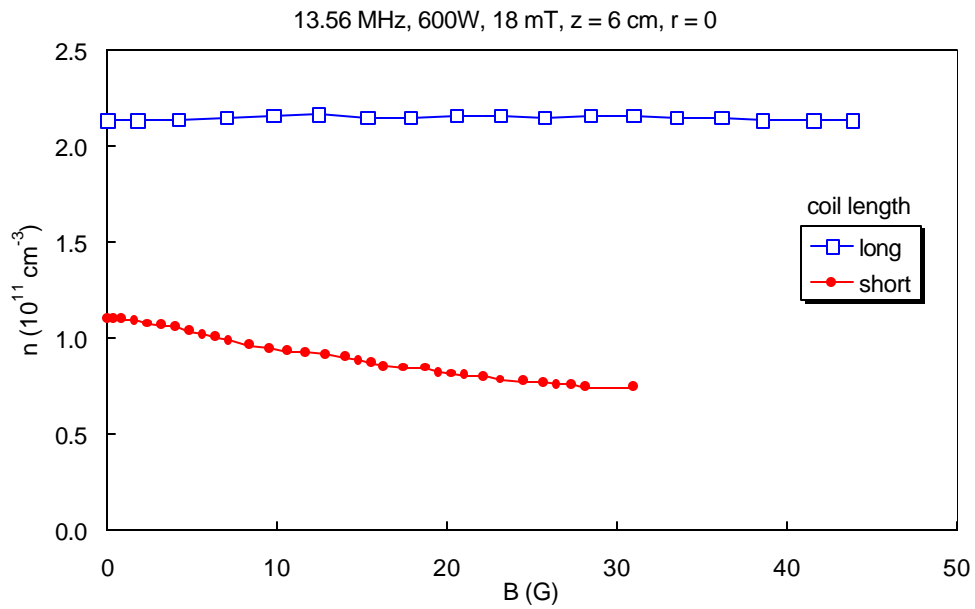


Fig. 16. Density vs. magnetic field for single- and double-length tubes.

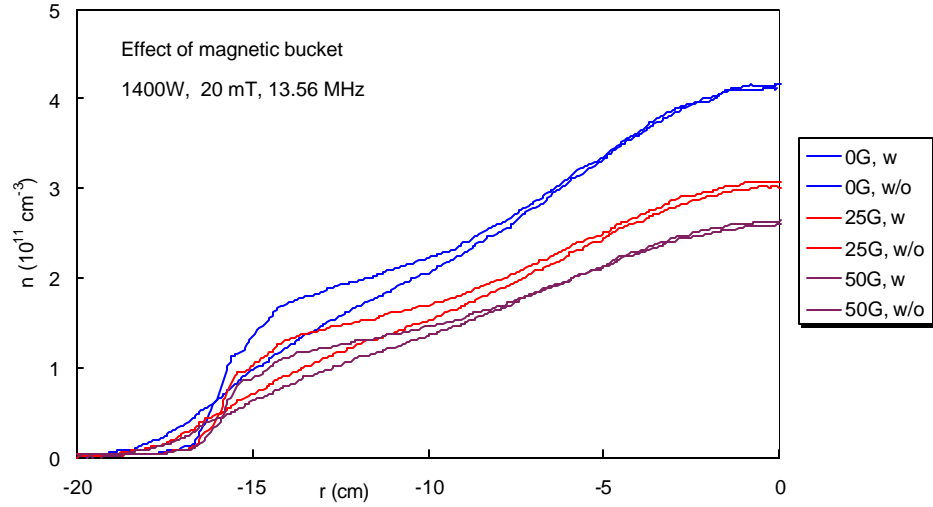


Fig. 17. Radial density profiles at three magnetic fields with (w, thick curves) and without (w/o, thin curves) a magnetic bucket in the experimental chamber. The curves are listed in the legend in the same order as they appear at the right of the graph.

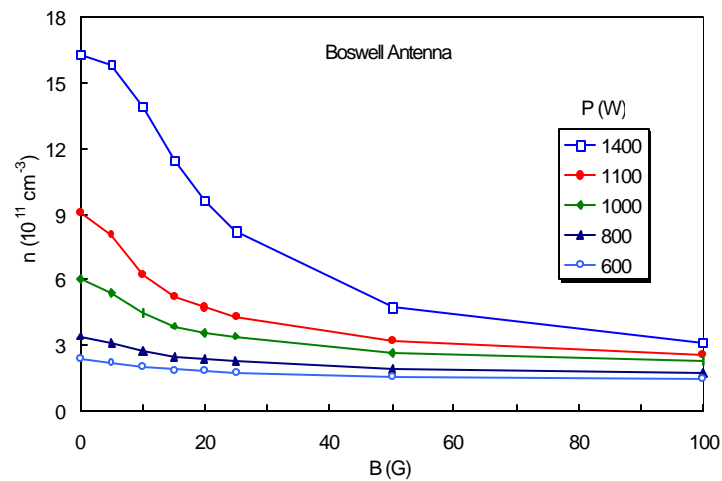
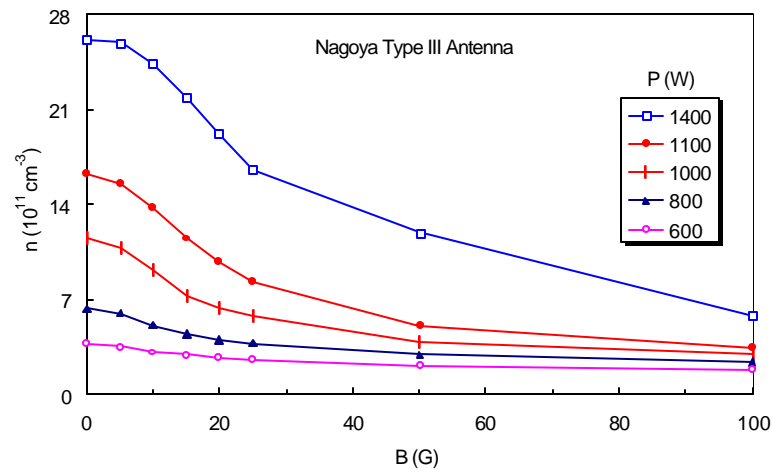


Fig. 18(a,b). Density vs. magnetic field and power for various antennas.

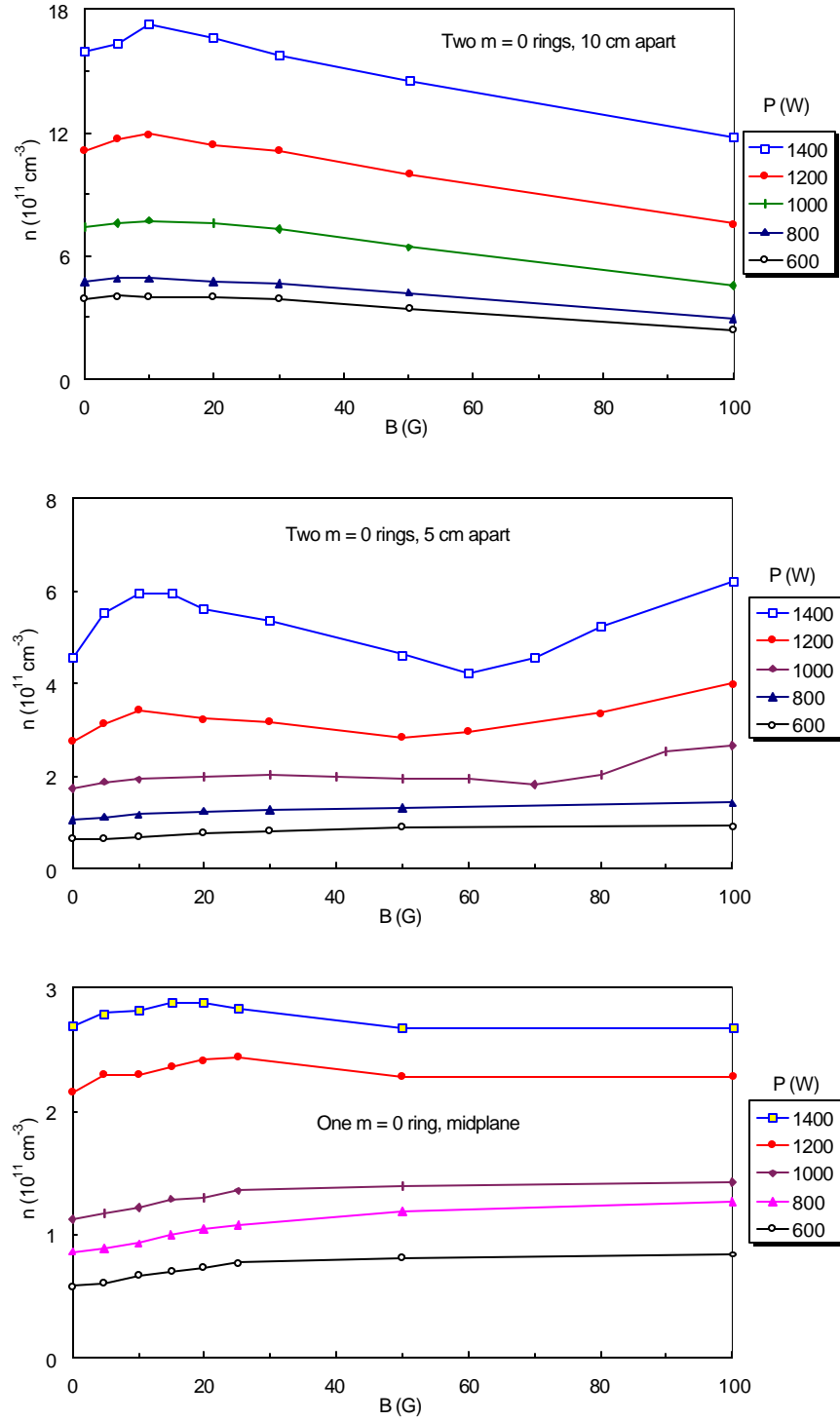


Fig. 18(c,d,e). Density vs. magnetic field and power for various antennas.

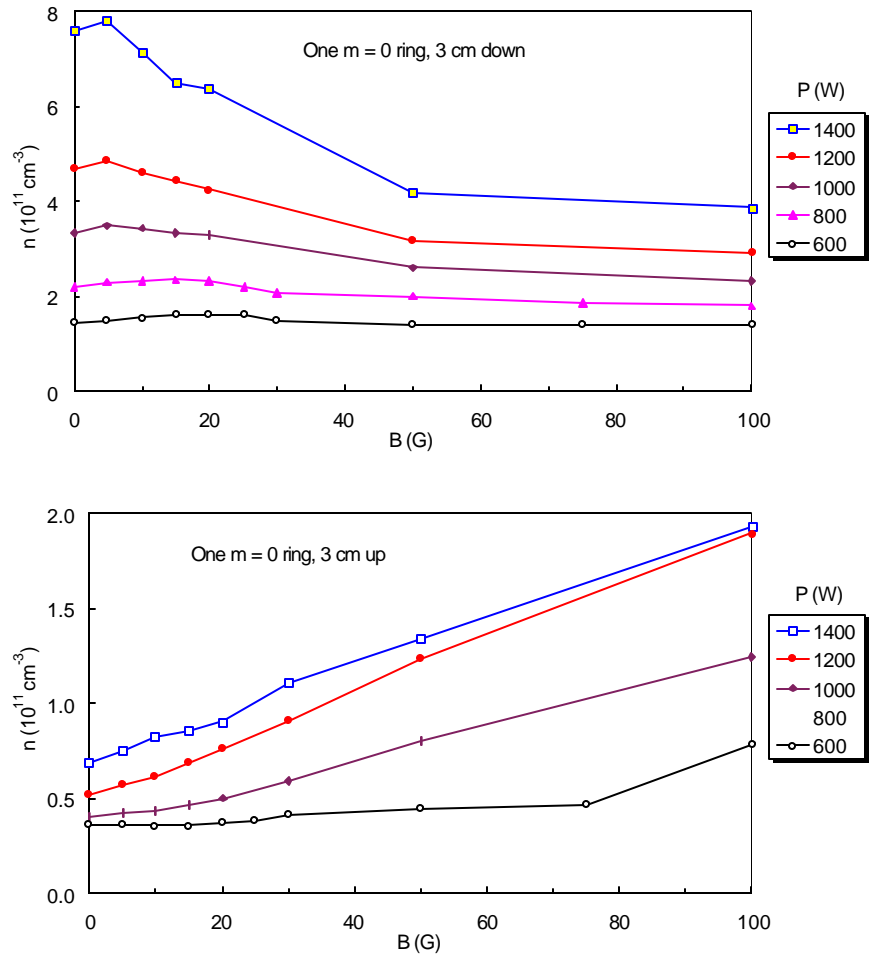


Fig. 18(f,g). Density vs. magnetic field and power for various antennas.

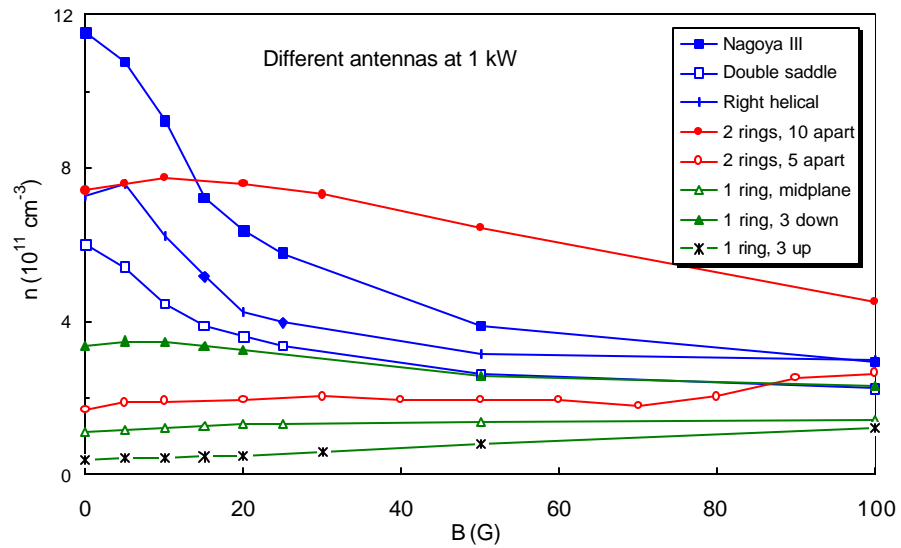


Fig. 19. Comparison of various antenna types at 1 kW power.

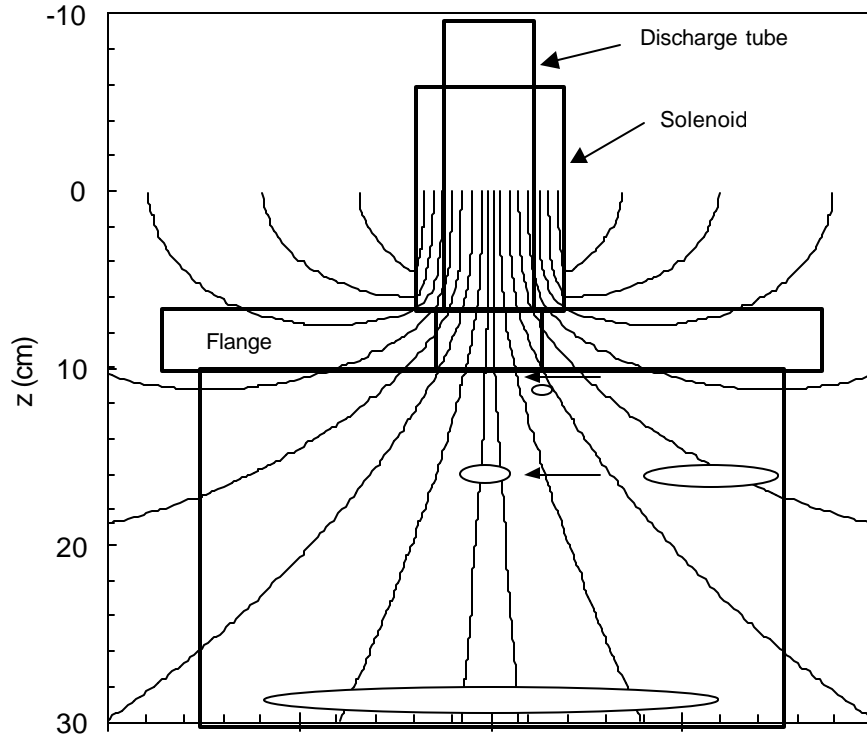


Fig. 20. Magnetic field lines in the present experiment. The arrows indicate the positions of the probes. The ellipses show the approximate sizes of the electron Larmor diameters at various positions when the field in the source on axis is 100G.

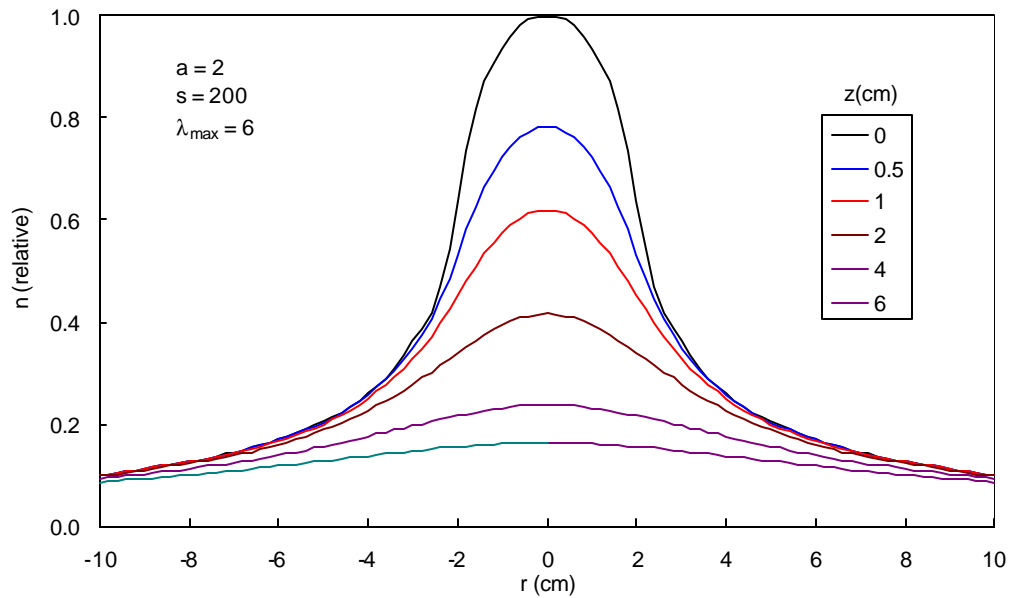


Fig. 21. Computed density profiles at various positions z for isotropic diffusion with $B = 0$.

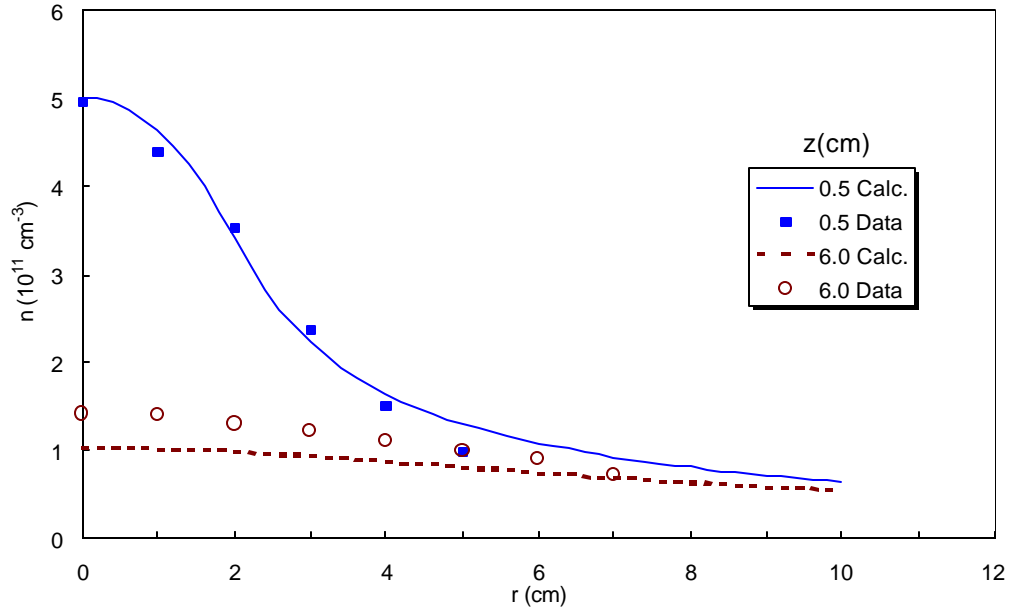


Fig. 22. Calculated diffusive radial profiles compared with the data of Fig. 13.

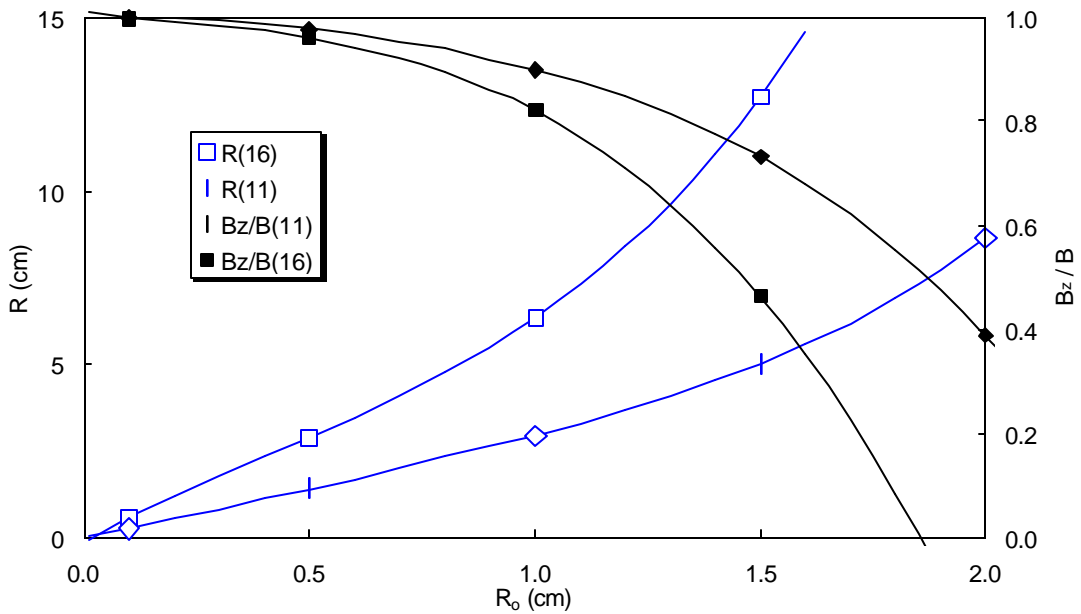


Fig. 23. Radius of field line at the probe positions $z_0 = 10.6$ and 16.1 cm from coil midplane ($z = 0.5$ and 6.0 cm from top flange), as function of midplane radius R_0 (hollow points). Also shown is $B_z/B = \cos q$, where q is the angle of the field line with the z axis (solid points).

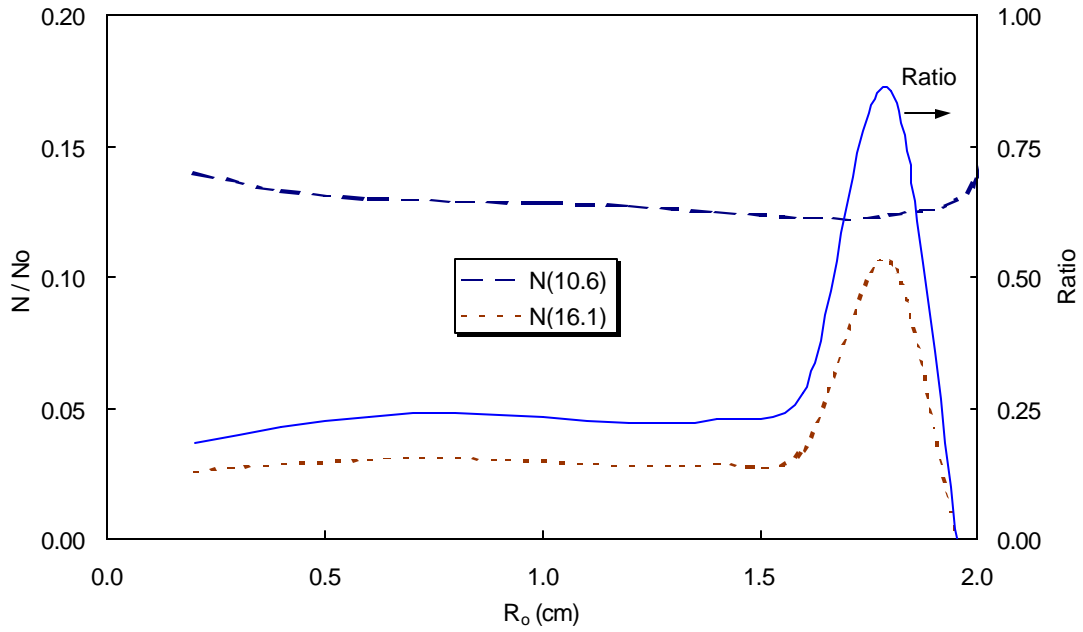


Fig. 24. Computed densities at the two probe positions and their ratio (solid line) for the case $B \rightarrow \infty$.

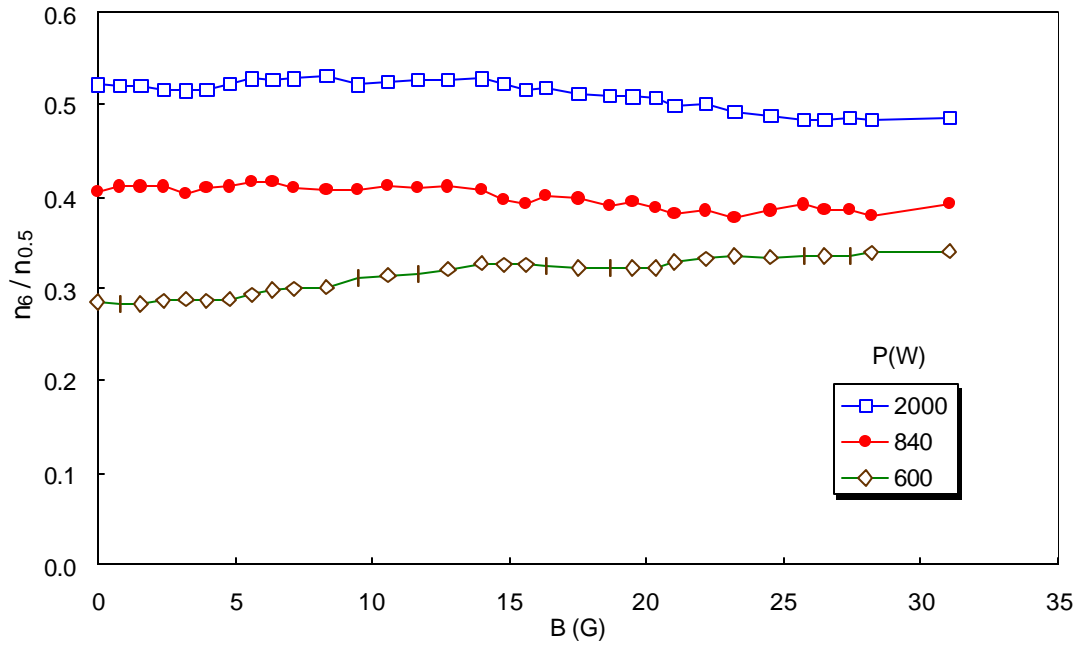


Fig. 25. Ratio of peak densities at $z = 6$ and 0.5 cm as function of magnetic field and power at 27.12 MHz (from data of Fig. 14).

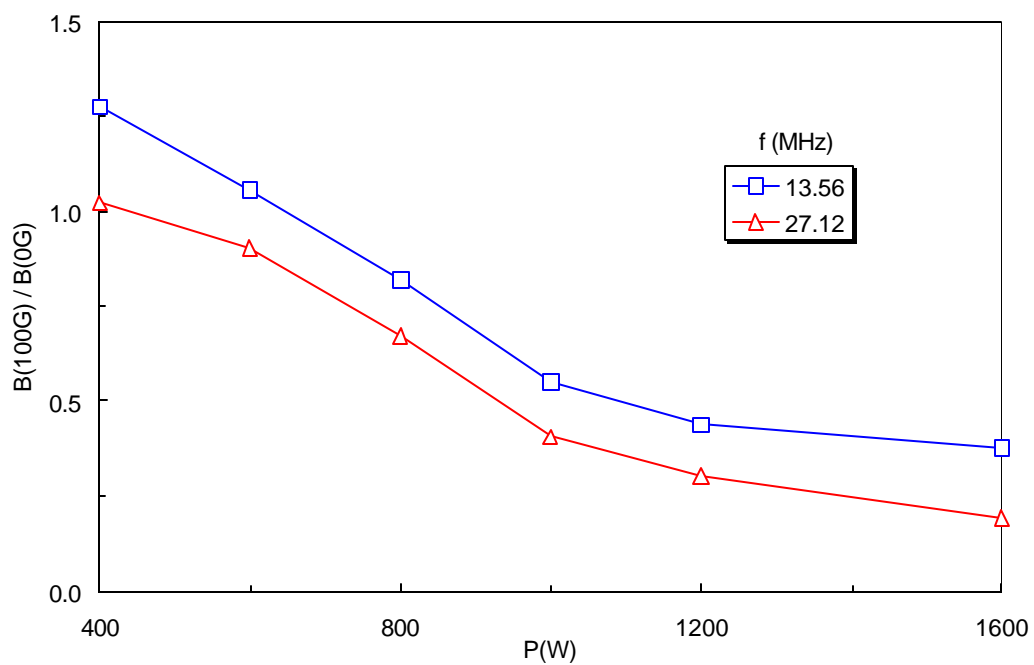


Fig. 26. Ratio of peak densities at 100G and 0G as a function of power at two frequencies.

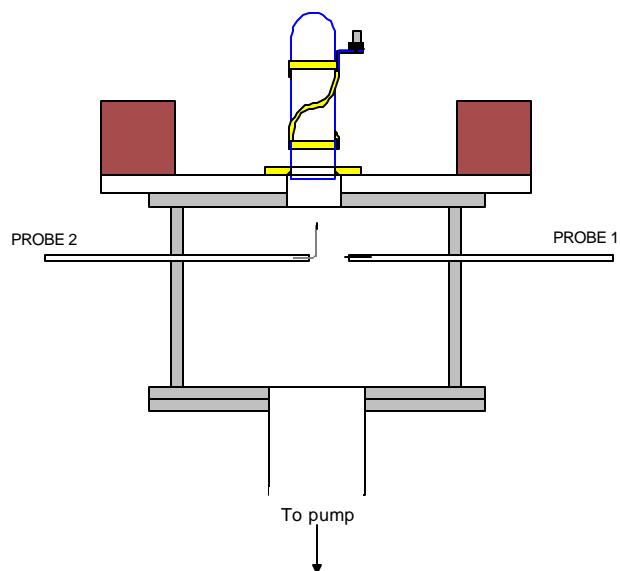


Fig. 27. Schematic of apparatus with large magnetic field coil.

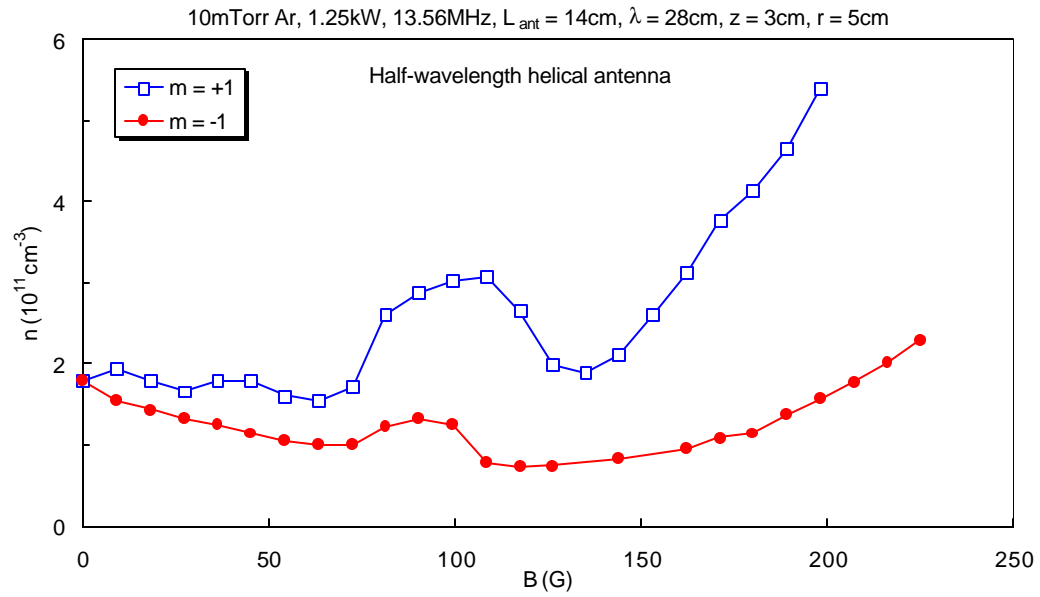


Fig. 28. Density vs. magnetic field with a helical antenna and the large field coil shown in Fig. 27.

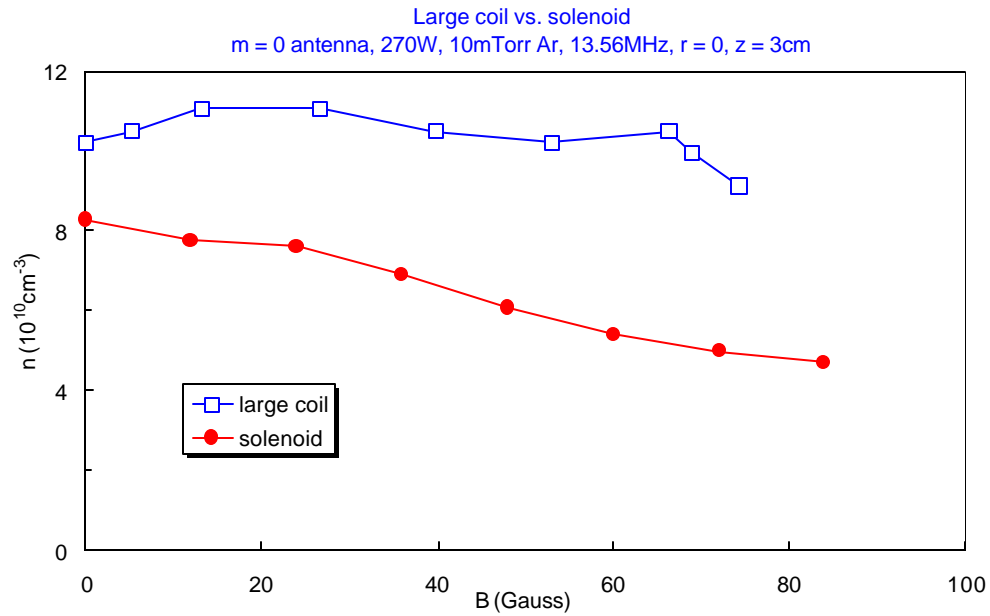


Fig. 29. Comparison between $n - B$ curves taken with a small solenoid and with a large coil, taken with an $m = 0$ antenna.